

Effect of voltage on second-stage electrodes of dual-stage solid propellant pulsed plasma thruster



Yueh-Heng Li^{a,*}, Clémence Royer^{a,b}

^a Department of Aeronautics and Astronautics, National Cheng Kung University, Tainan, 70101, Taiwan, ROC

^b Institut Polytechnique des Sciences Avancées, Paris, France

ARTICLE INFO

Keywords:

Dual-stage pulsed plasma thruster (PPT)
Electric propulsion (EP)
Late-time ablation (LTA)

ABSTRACT

A dual-electrode-stage PPT (DESPPT) using solid propellants has been developed with simple parallel electrodes and a deflected angle of 20°. By setting and testing different possible energy efficiencies, experiments were performed with one-stage and two-stage PPTs under high vacuum conditions ($\sim 10^{-5}$ Torr). The experiments revealed that increasing prototype second-stage energy leads to an increase in total impulse bit. Because a single-electrode-stage PPT has been demonstrated to only require approximately 60% ablated propellant to accelerate plasma, the dual-stage regimen might increase the percentage of mass that is ablated propellant. In other words, increasing the exhaust velocity and total impulse bit may be achievable by reusing late-time ablation with the dual regimen. A maximum total impulse bit of 72.35 $\mu\text{N}\cdot\text{s}$ has been obtained with the dual-mode prototype when 25 J of total energy is released through the thruster discharge chamber.

1. Introduction

For several decades, the development of satellites has been dominated by governments, large corporations, and institutions [1]. Traditional satellites are extremely large and bulky (typically weighing thousands of kilograms), and have high cost and power consumption. A new concept of miniaturized satellites has become prevalent due to the advantages of maneuverability and low capital cost. A vital characteristic of small satellites is that they can choreographically establish virtual networks and deliver higher resolution than large satellites. For example, a constellation of small satellites may employ some devices that collect data individually. This method augments signal quality and reduces the risk of satellite deterioration [2]. In addition, each satellite in the constellation can possess its own propulsion system for attitude control or position-keeping maintenance. However, satellites with propulsion capability contribute excellent flexibility and interoperability for the constellation. Therefore, miniaturized satellites are particularly well suited for international cooperation, offering an observational system that can measure all characteristics of the target of interest and enable us to explore unknown regions in space [3].

Satellite categories are generally distinguished by the weight of the satellite. SmallSats are satellites in the range of 10 kg to 180 kg, whereas CubeSat range are categorized according to the function of their unit size: One unit (U) of CubeSat is equal to a cube with the

dimensions of 10 × 10 × 10 cm and a weight of 1.33 kg. A 1U CubeSat costs approximately US\$ 150 000, including its launch and production. Therefore, CubeSats usually have sizes such as 1.5, 2, 3, or 6–16 U. Multiple CubeSats can be assembled to satisfy mission requirements or functionalities. CubeSats have numerous practical applications, such as BRICSat-P [4], UWE4 [5], and FalconSAT-3 [6]. In addition to satellites developed by government agencies or for-profit companies, many CubeSats have been developed by academic institutions and small and medium enterprises. The National Space Program Office of Taiwan has deployed a constellation of satellites, Formosat-7/Cosmic-2, which includes 7 small satellites to conduct GPS research on the upper ionosphere, climate, and meteorology. The Taiwanese satellite constellation YamSat is a collection of picosatellites designed to fulfil simple short-duration spectroscopy missions. CubeSat and other types of microsatellites constitute one of the most promising strategies for future space exploration. A growing number of studies are focusing on the development of different technologies that might be capable of meeting the requirements of microsatellites. In its initial stage, CubeSat was expected to make space research accessible to a wide range of organizations and universities; thrusters were thought to be unnecessary. Initial plans assumed that external forces would be sufficient to move the CubeSats so that they could perform experiments.

Newly updated CubeSat requirements specify the inclusion of thrusters to enhance mobility and maneuverability. These microengines

* Corresponding author. Department of Aeronautics and Astronautics, National Cheng Kung Univ., Tainan, 70101, Taiwan, ROC.

E-mail address: yueheng@mail.ncku.edu.tw (Y.-H. Li).

<https://doi.org/10.1016/j.vacuum.2019.05.037>

Received 17 March 2019; Received in revised form 27 May 2019; Accepted 28 May 2019

Available online 31 May 2019

0042-207X/ © 2019 Elsevier Ltd. All rights reserved.

can satisfy new investigative requests. Attitude control, orbit change, and group behaviors are crucial features for expanding the range of applications. Various propulsion systems for small cuboidal satellites have been developed, such as ion engines, pulsed plasma thrusters (PPTs), hall thrusters, and chemical propulsion systems. In general, propulsion systems in microscale satellites belong to the categories of either chemical propulsion (CP) or electrical propulsion (EP). Both of these systems have demonstrated excellent and highly efficient results but with certain weaknesses. EP consumes less propellant than does CP. Electrical power sublimates propellant by heating it to create plasma. It has a higher gas exhaust speed; however, downstream of the EP system, the thrust is much weaker than CP. Thus, EP systems can provide small thrusts for long-lasting operation, establishing them as suitable for different applications, such as fast maneuvers, orbit transfer, planetary escape, or interplanetary travel. In general, the EP mechanism can be categorized based on the ion acceleration mechanism into three types: *electrothermal*, *electrostatic*, and *electromagnetic* mechanisms [7].

PPT systems belong to the electromagnetic propulsion group [8]. They apply a mechanism in which stored energy is discharged quickly through an ionized medium in short pulses that are repeated at a controlled frequency. PPT is one of the most promising propulsion systems for CubeSat [9,10]. Physically, plasma acceleration is processed by a perpendicular combination of magnetic and electric fields. A Lorentz Force is induced and mainly used to accelerate the bulk in the nozzle. An external high-voltage capacitor, located above the anode (+) thruster, is charged. A sparkplug, located on the cathode, is used to create an electric arc. This electrical path comes into contact with the electrode near the Teflon surface to heat it and strip electrons from the propellant. This ionization process creates a medium. When the PPT chamber has been sufficiently ionized, the capacitor rapidly releases energy and the current flows between the two electrodes. The resulting magnetic and electric fields accelerate the plasma bulk along the nozzle because of the Lorentz force. Regarding fuel, PPT systems can be divided into gaseous-fuel PPT [11], liquid-fuel PPT [12,13], and solid-fuel PPT [14,15]. The thrust ranges from 0.3 to 0.75 mN, and the resulting specific impulse spans from 830 to 1200 s. Consequently, total impulse reaches 15 000 to 20 000 N s [16].

The optimal efficiency and performance of the thruster are determined as functions of the thruster geometry. The discharge chamber shape generally requires an adequate volume as well as a specific material and electrode configuration. Many types of EP systems already exist. Several relevant electrode models can be studied to enhance acceleration and exploit pinch acceleration effects, such as parallel electrodes, coaxial electrodes, and flared electrodes. During the discharge process, plasma mass is accelerated by the Lorentz Force; however, a second bulk of electrical material is quickly created before evolving more slowly in the discharge chamber. This second process is referred to as late-time ablation (LTA) and does not contribute to the thrust efficiency downstream of the thruster [17]. In articles describing this process, certain assumptions are made after the initial electromagnetic acceleration step: the propellant ablation process continues after discharge because of the heat. Propellant continues to be consumed after the current stops flowing. Charged particles and macro particles are ejected from the discharge chamber at a velocity lower than the first velocity. This mass overage cannot be used and is lost. Indeed, adding another set of electrodes downstream of the first electrode set may be a solution for utilizing this lost plasma mass to increase the thrust and obtain more benefits. This idea led us to design the dual-electrode-stage PPT (DESPPT), which demonstrates superior efficiency and performance compared with a single-stage PPT. Considering that a simple PPT only uses approximately 50% of the ionized solid propellant to accelerate plasma and create thrust, this dual-electrode-stage model accelerates the reduction in ionized mass of the propellant, namely LTA, by contributing a second burst of energy from a second capacitor to increase thrust efficiency [18]. The operation is simple because it resembles the first operation in which an ionized medium reaction mass

is produced from the initial process. Following this principle, a second sparkplug and second solid propellant are unnecessary for the second stage. The second discharge is then triggered by itself with a certain time delay depending on the amount of supplied energy.

2. DESPPT design and measurement method

2.1. Design of the DESPPT and electrical supply circuits

A DESPPT prototype was designed using Teflon as the propellant and electrodes fabricated from Cu with a thickness and width of 2 and 15 mm, respectively. The first-stage electrodes had a length of 32 mm, and the projected length of the second-stage electrodes was 22 mm. The second-stage electrodes consisted of a 5-mm flat plate and 18.41-mm deflected plate with a deflection angle of 20°. The selection of electrode with a deflection angle of 20° is advised from the literature [19], which discovered the PPT with 20° flared angle had the highest efficiencies compared to PPT without flared angle. The electrode gap was 24 mm, and the distance between the first-stage and second-stage electrodes was 10 mm. A small Cu rod was designed and insulated from the cathode using Teflon. This Cu rod (diameter of 3 mm) served as the initiator for the thruster. Screws were used to connect the electrodes to the cables. Quartz was used to support the electrodes and served as the side walls. Two Teflon frames were used to clip the electrodes and quartz. Fig. 1 displays the schematic and photograph of the proposed DESPPT prototype.

All tests in this study were conducted in a stainless-steel cylindrical vacuum chamber with dimensions of 50 × 60 mm² (diameter × length). The pump system comprised an oil-free scroll dry pump (PTS06003 UNIV, Agilent Technologies Inc, Santa Clara, CA, USA), a turbo molecular pump (HIPace 80, Pfeiffer Vacuum GmbH, Asslar, Germany), and a water cooling system. Pressure conditions varied from 10⁻⁴ to 10⁻⁶ Torr. The dry pump was used first to decrease the chamber pressure to less than 0.05 Torr, and then the turbo molecular pump was used to achieve medium vacuum (MV, 0.75–7.5 × 10⁻⁴ Torr) and high vacuum (HV, 7.5 × 10⁻⁴ to

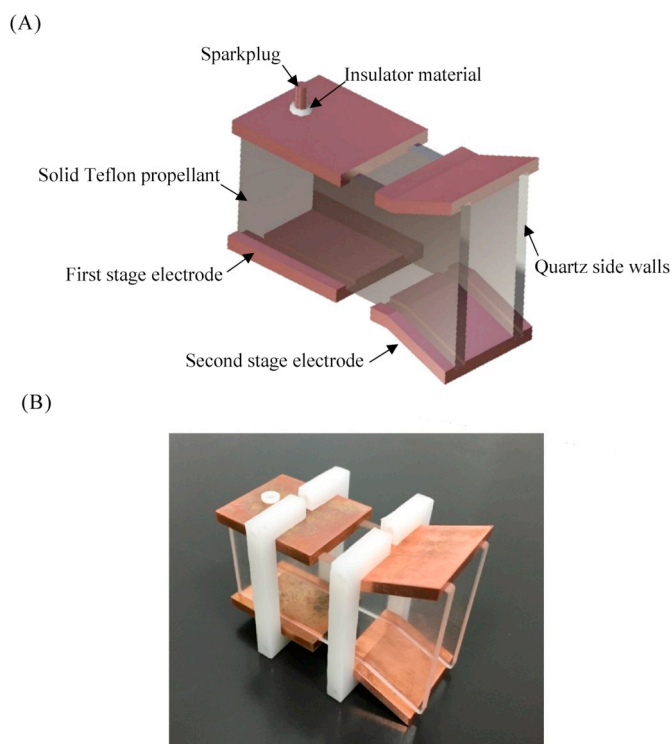


Fig. 1. (A) Schematic of the DESPPT and (B) photograph of the DESPPT.

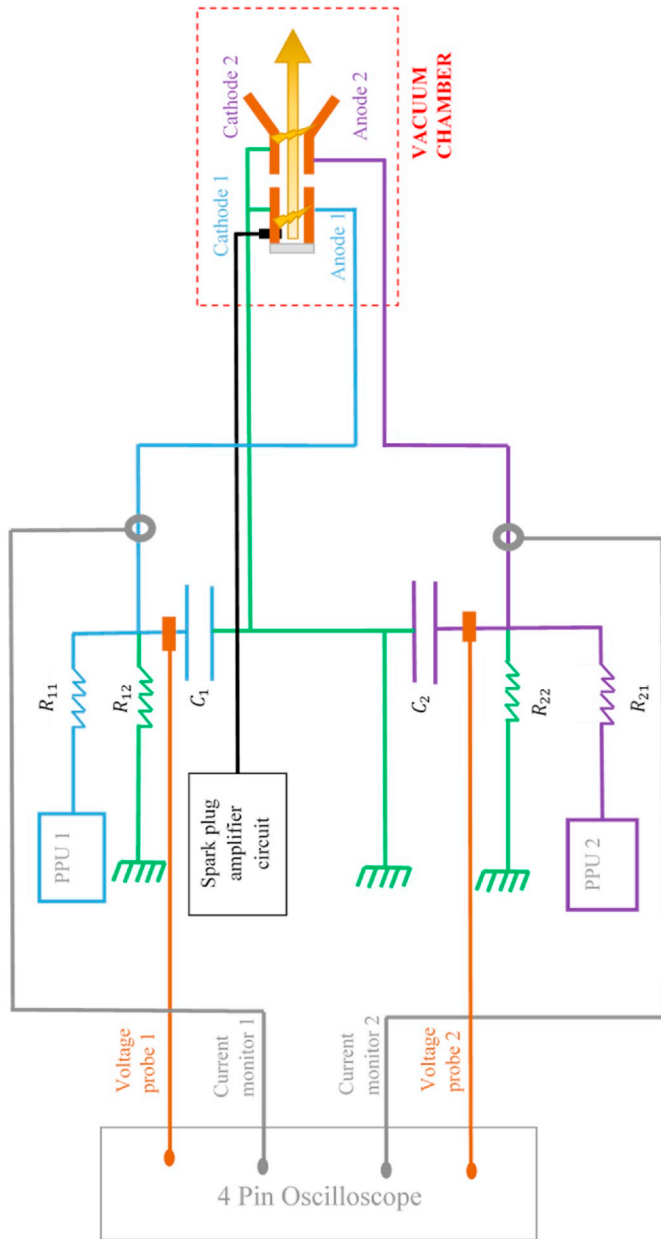


Fig. 2. Diagram of the electrical circuit to supply the DESPPT system.

7.5×10^{-8} Torr) conditions. Pressure readings were obtained using a vacuum gauge (Penningvac PTR 90 N, Leybold GmbH, Cologne, Germany), which enabled atmospheric pressure to be measured up to 1×10^{-9} Torr using a single transmitter. The entire vacuum system used an automatic control system to achieve switching and used a display panel for immediate monitoring and operation. Pressure conditions varied in the range of 10^{-4} to 10^{-6} Torr for simulating the low-orbit vacuum conditions of Earth.

Regarding the electrical supply circuit for DESPPT, three distinct electrical circuits were required: one for the sparkplug, one for the first-stage electrodes, and one for the second-stage electrodes. Fig. 2 presents the electrical circuits for the DESPPT system. Two 6-W power supplies were used. The basis of PPT operation is the utilization of a high voltage to obtain a high peak current as well as high energy and thrust. The prototype was then tested for different voltage ranges, and the requested power system was determined in appendix.

The spark plug is connected to an amplifier circuit fed by a 12-V battery. The output voltage from a downward amplifier circuit is

approximately 6000 V. The components involved in the first-stage and second-stage circuits are similar. Thus, a single circuit contains one 25- μ F capacitor and two distinct resistances. The first resistance, which comes directly downward from the positive output of the power supply unit, is essential; it protects the power supply in case of poor current flow. As we know, high current is used to feed the thruster; therefore, the design should anticipate the case in which current flow is reversed. Without this resistance, such unexpected current could damage the power supply. The second resistance is located in parallel and directly connected to the ground. This secondary resistance must be protected in case the discharge fails and the energy is not released within the discharge chamber. When the sparkplug is triggered, discharge occurs between electrodes. If the discharge fails, the energy remains in the capacitor. Again, because a high current is used, it is notably dangerous. In a laboratory setting, precautions should be taken to prevent the discharge from coming into contact with the laboratory researchers. Adding this secondary resistance will force the current to discharge directly into the ground and not in an unexpected area.

The first resistance value must be sufficiently high to protect the power supply. Therefore, the first resistance can be determined as follows:

$$R = \frac{V^2}{P} \text{ [}\Omega\text{]} \quad (1)$$

Thus, first-stage and second-stage resistances must be at least:

$$R_1 = \frac{1000^2}{6} = 166 \text{ [k}\Omega\text{]} \quad (2)$$

$$R_2 = \frac{500^2}{6} = 42 \text{ [k}\Omega\text{]} \quad (3)$$

To maintain the two power supply units, the selected resistance values are as follows:

$$R_{11} = 1 \text{ [M}\Omega\text{]} \text{ and } R_{21} = 100 \text{ [k}\Omega\text{]}$$

The circuit is set as a voltage following operational amplifier. To determine the second resistance value, the following equations of the voltage divider can be processed.

2.2. First the capacitor impedance is defined as follows

$$Z_c = \frac{1}{j\omega C} \text{ with } C=25 \mu\text{F}$$

According to Kirchhoff's law and electric circuit equations, the capacitor impedance does not influence the transfer function. Therefore, the output voltage is equal to

$$V_{in} = \frac{Z_c | R_2}{Z_c | R_1 + R_2} \times V_{out} \text{ [V]} \quad (4)$$

$$V_{in} = \frac{R_1 + R_2}{R_2} \times V_{out} \text{ [V]} \quad (5)$$

As we know, $R_{11} = 1 \text{ M}\Omega$ and $V_{in1} = 1000 \text{ V}$, and we aim to achieve the same output voltage between the electrodes ($V_{out1} \approx 1000 \text{ V}$).

The second resistance value must be approximately 100 times higher. Indeed, in the early days of ion engine construction, two similar resistances were used on the second electrode stage, and the final output voltage between electrodes was divided by two. This led to problems in terms of resistance. Therefore, the second resistance value has been made 100 times greater to avoid halving the output voltage. The secondary resistance is thus as follow:

$$R_{12} = R_{11} \times 100 = 100 \text{ [M}\Omega\text{]} \quad (6)$$

For the second stage, $R_{21} = 100 \text{ k}\Omega$, the applied voltage is generally $V_{in2} = 200 \text{ V}$, and we aim to achieve the same output voltage between the electrodes ($V_{out2} \approx 200 \text{ V}$). Then, the secondary resistance is:

$$R_{22} = R_{21} \times 100 = 10 [M\Omega] \quad (7)$$

Table 1 shows the all parameters of DESPPT, and the determination of these parameters are presented in Appendix.

2.3. Measurement system

Because a PPT is an electromagnetic engine for space applications, accurate high-voltage probes should be used to determine relevant performance measurements of the device. The DESPPT is subjected to high currents, and the probe measurement range should be selected accordingly. Otherwise, the saturation edge will be surveyed, which can negatively affect or distort data measurement. Voltage probes are passive devices with adjustable attenuations of $\times 1$, $\times 10$, $\times 100$, or $\times 1000$. All voltage probes are supposed to measure signal with minimal perturbation by avoiding electromagnetic noise coming from the surrounding apparatus and other systems. Additionally, induction effects can induce perturbation between two wires. This results from electromagnetic flow and potential differences, which induce an electromotive force and thus lead to disruptions in the current. The voltage probe used to integrate measurements was a PINTEK HVP-15HF high-voltage probe with a 15-kV discharge current and 30-kV peak current. The attenuation was fixed at the $\times 1000$ ratio. Another probe, namely a TEKTRONIX P6015A 20-kV discharge current and 40-kV peak current high-voltage probe with $\times 1000$ attenuation, was simultaneously used to measure voltage from the second stage.

Low-voltage probes have also been used to measure triple Langmuir probe (TLP) potential for investigation of electron density. A current probe is an active probe; its operation is based on the Hall effect principle. This theory can be applied to measuring magnetic field variations with inductive sensing devices; a magnetic circuit exists between the desired wire (which is a primary conductor) and a coil (which is the secondary conductor). The interaction of magnetic fields induces variations, which enables the measurement of current intensity. Two current probes were used to perform experiments: a low-current probe Yokohama CTL-35-S162-5F-1R10 of $\times 10$ attenuation and a high-current Pearson monitor with $\times 100$ attenuation, sensitivity of 0.01 V/A, and peak current of 50 kA. The oscilloscope used was a 200-MHz Tektronix DPO 2024B Digital Phosphor Oscilloscope. This 4-pin oscilloscope was highly convenient for our experiments. Power supplies were Matsusada ES-5R1.2 LG and ES-1R6 generators. The voltage limits were fixed at 5 kV and 1 kV, respectively; the output currents were 1.2 mA and 6 mA; and output power for both devices was 6 W.

A triple Langmuir probe was used to assess the efficiencies and characteristic parameters of the DESPPT. The operation of the probe is based on the measurement of potential difference between three parallel probes placed downstream of the thruster exhaust. From triple Langmuir probe voltage samples, plasma density and electron temperature can be obtained using equations. Biased voltage is induced between two probes that are exposed to the exhausted plasma. Hence, when the plasma bulk comes into contact with the exposed wires, it creates a current flowing through the circuit of these two connected wires. The remaining wire floats.

Voltage is induced between probe 3 and probe 1 while probe 2 floats.

$$V_{d_2} = |V_1 - V_2| [V] \quad (8)$$

$$V_{d_3} = |V_1 - V_3| [V] \quad (9)$$

The floating probe is not grounded; thus, the voltage curve acquired from probe 2 only measures the potential difference of the plasma sheet. The curve amplitude is low and has one oscillation greater than 0 V. Voltage from the two biased probes (1 and 3) reflects the potential difference between the applied battery voltage and plasma sheet. Because biased probes are grounded, the curve presents few voltage oscillations at high potential, fluctuating between positive and negative

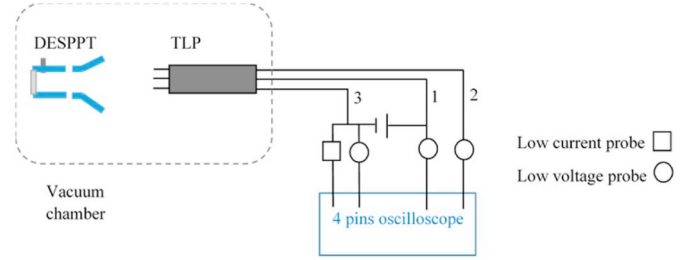


Fig. 3. Block diagram of the Langmuir Triple Probe set up.

potentials. The density is determined from the difference in potential between the applied voltage probe and the floating probe. The final electron density and temperature is given by the following equations [20].

$$T_e = \frac{eV_{d_2}}{k \log(2)} \quad (10)$$

$$n_e = \frac{-I_1}{eZS_p \sqrt{\frac{kT_e}{m_i}} e^{0.5}} \frac{\exp\left(\frac{-eV_{d_2}}{kT_e}\right)}{1 - \exp\left(\frac{-eV_{d_2}}{kT_e}\right)} [m^{-3}] \quad (11)$$

Probe wires were made from tungsten material with a diameter of 0.3 mm. The effective probe length was 0.8 mm, and each probe was separated from the closest probe by a distance of 3 mm. We supplied 27 V from three batteries in a series of 12 V to 4 Ah and 6 V to 3 Ah. The distance from the top of the probes and DESPPT exhaust area was maintained at 2 cm, as shown in Fig. 3.

To document the entire discharge process, a high-speed camera (FASTCAM SA5) was used to capture the discharge process of pulsed plasma thruster [21]. The FASTCAM SA5 high-speed camera could shoot up to 300 000 frames per second, but the resolution was low (128×16 pixels). After adjustment, the minimum resolution required to observe the entire thruster surface was 512×288 pixels. The camera was configured at 72 000 frames per second (resolution 512×288 pixels) and a lens (Nikon AIS 85 mm) was arranged to capture images. At 72 000 frames per second, a new image was shot every 13.88 μ s. In addition, a narrow 308 nm-band pass filter was arranged with the high-speed camera to reduce the brightness of discharge and facilitate clear photography of the plasma flowing into the discharge chamber.

3. Results and discussion

3.1. Determination of thrust efficiency based on voltage breakdown and peak current

The amount of thrust produced downstream of the thruster was the product of the impulse bit and pulse frequency. The equations for the thrust and impulse bit are as follows:

$$T = I_b \times f [N] \quad (12)$$

$$I_b = \frac{\mu h}{2w} \int_0^\infty i^2(t) dt [\mu N \cdot s] \quad (13)$$

where h is electrode gap, w is electrode width, μ is magnetic permeability, and $i(t)$ is the instantaneous discharge current. To determine the impulse bit, we were required to first obtain the integral under the square of instantaneous discharge current curve function of the time, that is, $i^2(t)$. By using Origin Pro 9 software, plotting and determining this value is a straightforward process. Then, the total impulse bit is given by the sum of the two-stage impulse bit.

$$I_{b_{tot}} = I_{b1} + I_{b2} [\mu N \cdot s] \quad (14)$$

According to the two-stage voltage graphs, we can determine Δt between the two rising edges. Thus, we can calculate the exhaust

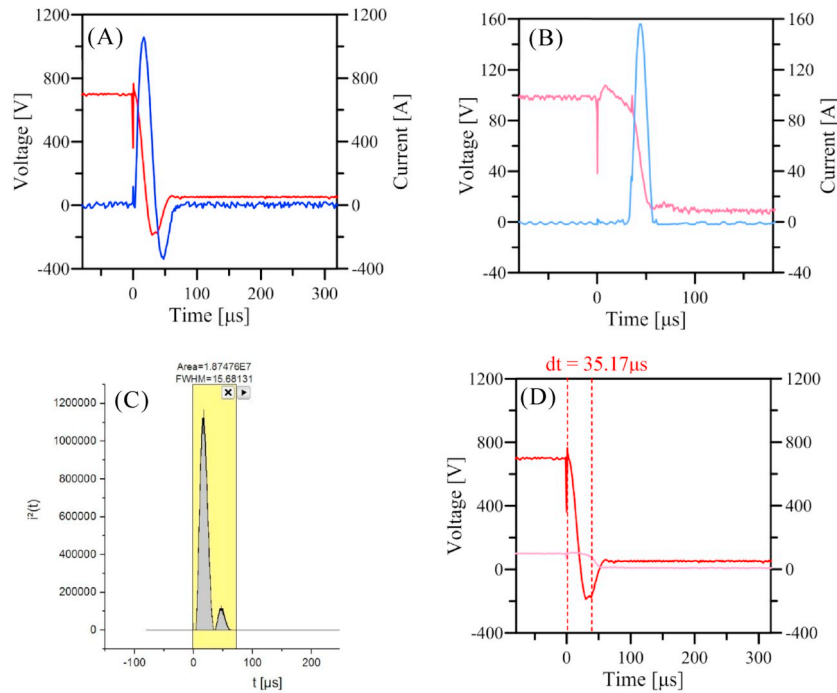


Fig. 4. Distribution history of voltage and current at (A) first-stage cathodes supplied by 700 V and (B) second-stage cathodes supplied by 100 V. (C) Determination of the integral of $i^2 \Delta t$ of first-stage cathodes. (D) Determination of the discharging period between first-stage and second-stage cathodes.

velocity of the plasma coming out from the first stage and reaching the second electrode set.

$$v_e = \frac{\Delta x}{\Delta t} \text{ [m/s]} \quad (15)$$

Experimental assumptions can be made regarding the ablated mass and specific impulse. Because the propellant requires contact and ionization only once to induce the two-stage discharge, we can find the ablated mass value along with the approximate exhaust velocity and impulse bit value. Only first-stage data are required to determine these values. The following equations describe performance in terms of ablated mass, specific impulse, exhaust velocity, and thrust efficiency.

$$m_a = \frac{I_b}{v_e} \text{ [\mu g]} \quad (16)$$

$$I_{sp} = \frac{v_e}{g} \text{ [s]} \quad (17)$$

$$\eta_t = \frac{1/2 \cdot m_a v_e^2}{E_t} \text{ [%]} \quad (18)$$

For example, the first-stage cathodes were charged with 700 V, the second stage cathodes were charged by 100 V. Fig. 4(a) and (b) show the distribution histories of current and voltage, respectively. Fig. 4(c) demonstrates the determination of the integral of $i^2(t)$ with Origin Pro 9. Every impulse bit can be determined with (13). Then, for this first test, the first-stage impulse bit is as follows:

$$I_b = \frac{\mu \times 24}{2 \times 15} \times 1.875 \times 10^7 \text{ [\mu N \cdot s]} \quad (19)$$

$$I_{b1} = \frac{16\pi}{5} \times 1.876 = 18.86 \text{ [\mu N \cdot s]} \quad (20)$$

whereas the second-stage impulse bit is

$$I_{b2} = \frac{16\pi}{5} \times 0.02558 = 0.257 \text{ [\mu N \cdot s]} \quad (21)$$

By determining the location of peak current and breakdown voltage, determining the discharging time is a straightforward process.

Table 1
DESPPPT experimental parameters.

| Parameter | Value |
|--|--|
| Power supply 1 | $P_1 = 6 \text{ [W]}$ |
| Power supply 2 | $P_2 = 6 \text{ [W]}$ |
| Capacitor 1 | $C_1 = 25 \text{ [\mu F]}$ |
| Capacitor 2 | $C_2 = 25 \text{ [\mu F]}$ |
| Charging voltage range 1 | $V_1 = 500 \text{ to } 1000 \text{ [V]}$ |
| Charging voltage range 2 | $V_2 = 150 \text{ to } 1000 \text{ [V]}$ |
| Power supply protection resistance 1 | $R_{11} = 1 \text{ [M}\Omega\text{]}$ |
| Safety resistance 1 | $R_{12} = 100 \text{ [M}\Omega\text{]}$ |
| Power supply protection resistance 2 | $R_{21} = 100 \text{ [k}\Omega\text{]}$ |
| Safety resistance 2 | $R_{22} = 10 \text{ [M}\Omega\text{]}$ |
| Minimum energy on the first stage | $E_{500V1} = 3.125 \text{ [J]}$ |
| Minimum energy on the second stage | $E_{150V2} = 0.281 \text{ [J]}$ |
| Maximum energy on the first and second stage | $E_{1000V} = 12.5 \text{ [J]}$ |
| Total capacitor charging time | $T = 125 \text{ [s]}$ |

Accordingly, the discharging period between first-stage and second-stage cathodes was determined to be 35.17 μs, as shown in Fig. 4(d). The exhaust velocity of the plasma coming out from the first stage and

Table 2
Measured data energy breakdown and peak current when voltage for first stage and second stage electrodes are 700V and 100V.

| Parameter | Measured value | Determined value |
|-----------------|-----------------------|--|
| V_1 700 [V] | Δt 35.17 [μs] | $v_{e1} = \frac{\Delta x}{\Delta t}$ 1194 [m/s] |
| V_2 100 [V] | I_{b1} 18.86 [μN·s] | $m_a = \frac{I_{b1}}{v_{e1}}$ 15.8 [μg] |
| E_1 6.125 [J] | I_{b2} 0.257 [μN·s] | $I_{sp1} = \frac{v_{e1}}{g}$ 121.71 [s] |
| E_2 0.125 [J] | | $v_{e2} = \frac{I_{b2}}{m_a}$ 16.28 [m/s] |
| E_t 6.250 [J] | | $I_{sp2} = \frac{v_{e2}}{g}$ 1.66 [s] |
| | | $I_{b,t} = I_{b1} + I_{b2}$ 19.117 [μN·s] |
| | | $\eta_t = \frac{1/2 m_a v_{e1}^2}{E_t}$ 0.18 [%] |

Table 3

Data measurement from energy breakdown and peak current when voltage for second-stage electrodes remains constant at 800 V.

| V_2 [V] | E_1 [J] | E_2 [J] | E_t [J] | Δt [μ s] | V_{e1} [m/s] | V_{e2} [m/s] | m_a [μ g] | I_{b1} [μ N·s] | I_{b2} [μ N·s] | $I_{b,t}$ [μ N·s] | $I_{sp,1}$ [s] | $I_{sp,2}$ [s] | η_t [%] |
|-----------|-----------|-----------|-----------|-----------------------|----------------|----------------|------------------|-----------------------|-----------------------|------------------------|----------------|----------------|--------------|
| 0 | 8 | 0 | 8 | 27 | 1556 | 0.12 | 17.1 | 26.54 | 1.98 | 28.52 | 158.6 | 0.01 | 0.26 |
| 200 | 8 | 0.5 | 8.5 | 18 | 2333 | 0.29 | 9.3 | 21.64 | 2.7 | 24.34 | 237.9 | 0.03 | 0.30 |
| 400 | 8 | 2 | 10 | 9.2 | 4565 | 1.36 | 4.7 | 21.64 | 6.44 | 28.08 | 465.4 | 0.14 | 0.49 |
| 600 | 8 | 4.5 | 12.5 | 5.2 | 8077 | 4.58 | 2.7 | 21.64 | 12.28 | 33.92 | 823.3 | 0.47 | 0.70 |
| 800 | 8 | 8 | 16 | 3.4 | 12353 | 11.39 | 1.8 | 21.64 | 19.95 | 41.59 | 1259.2 | 1.16 | 0.84 |
| 1000 | 8 | 12.5 | 20.5 | 2.4 | 17500 | 25.79 | 1.2 | 21.64 | 31.89 | 53.53 | 1783.9 | 2.63 | 0.92 |

reaching the second electrode set can be assessed as follows.

$$v_e = \frac{\Delta x}{\Delta t} \text{ [m/s]} \tag{22}$$

where Δx is the distance between the two discharge locations, that is, 0.042 m. Eventually, the exhaust velocity can be expressed as

$$V_{e1} = \frac{0.042}{35.17 \times 10^{-6}} = 1194 \text{ [m/s]} \tag{23}$$

Presently, experimental assumptions can be made on the ablated mass and specific impulse. Because the propellant requires contact and ionization only once to induce the two-stage discharge, we can determine the ablated mass value along with the approximate exhaust velocity and impulse bit value. Only first-stage data are needed to determine those.

$$m_a = \frac{I_{b1}}{v_{e1}} = \frac{18.86 \times 10^{-6}}{1194} = 15.8 \text{ [\mu g]} \tag{24}$$

$$I_{sp1} = \frac{V_{e1}}{g} = \frac{1194}{9.81} = 121.71 \text{ [s]} \tag{25}$$

I_{bit} and v_e are calculated from real experimental values, but the equations are based on theory and are not impartial. Because the ablated mass remains the same for the two discharge voltages, we can deduce the exhaust velocity of the second stage.

$$V_{e2} = \frac{I_{b2}}{m_a} = \frac{0.2572}{15.8} = 16.28 \text{ [m/s]} \tag{26}$$

$$I_{sp2} = \frac{V_{e2}}{g} = \frac{16.28}{9.81} = 1.66 \text{ [s]} \tag{27}$$

Table 2 lists the measured values, such as impulse bit and Δt , and determined values, such as exhaust velocity, ablated mass per pulse, specific impulse, and thruster efficiency. $I_{sp1} \gg I_{sp2}$ because of the different voltages supplied to the first and second stages (see Table 1). Adding this second PPT allows the accumulation of the two impulse bit values to obtain a higher total impulse bit for the same amount of ablated mass.

3.2. Effect of voltage variation of second stage electrode on thruster performance

In order to assess the effect of voltage variation of second stage electrode on thruster performance, the voltage of the second-stage electrode set was varied from 0 to 1000 V, but the voltage of the first-

stage electrode set remained fixed at 800 and 1000 V. Tables 3 and 4 display the corresponding parameters. The results indicate that increasing the voltage of the second electrode could monotonically reduce the delay time, that is, increase the exhaust velocities when V_1 was fixed at 800 V. The total impulse bit ($I_{b,t}$) increased from 28.52 μ N·s (at $V_2 = 0$ V) to 53.53 μ N·s (at $V_2 = 1000$ V), and the resulting thrust efficiency improved from 0.26% (at $V_2 = 0$ V) to 0.92% (at $V_2 = 1000$ V). Although the impulse bit and thrust efficiency improved by an increase in voltage of the second-stage electrodes, the improvement does not justify the additional power input to the second-stage electrodes. However, when potential to the first-stage electrodes increased to 1000 V, the voltage of the second-stage electrodes changed to 200 V; the delay time increased, and the exhaust velocity from the first-stage electrode decreased correspondingly, as demonstrated in Table 4. Nonetheless, the voltage of the second-stage electrode reached 400 V and higher; the results resemble those of Table 3. The total impulse bit ($I_{b,t}$) increased from 41.09 μ N·s (at $V_2 = 0$ V) to 72.35 μ N·s (at $V_2 = 1000$ V), and the resulting thrust efficiency improved from 0.52% (at $V_2 = 0$ V) to 1.56% (at $V_2 = 1000$ V).

One trial reported a voltage supply of 1000 V to the first stage and 0 V to the second stage. This sample processed the thruster as a single-electrode-stage PPT. The delay time of the plasma toward the exit was 13.188 μ s

Different configurations are listed. A maximum impulse bit of 72.3 μ N·s was observed when two stages were supplied by 1000 V. The configuration supplied 1000 V in the first stage and 0 V in the second stage, which produced a lower impulse bit of 41 μ N·s. Additionally, a new phenomenon of plasma acceleration was observed. Δt was equal to 13.1 μ s when no second stage was added and decreased to 1.26 μ s when a second stage was supplied by 1000 V. Indeed, the Δt between the first stage and second stage decreased when the second-stage energy increased. Assumptions can be made based on these results; for example, adding a second electrode stage can induce another magnetic field that pulls particles toward the exhaust at a higher velocity. A comparison of the exhaust velocities in the two tables demonstrates the efficiency of the DESPPT. For example, for a 12.5-J energy single PPT, the velocity is 3184 m/s. When a two-stage DESPPT is supplied by 10 J (8 J on the first stage and 2 J on the second), the exhaust velocity is 4585 m/s, which is much higher and uses less energy. Similarly, for a two-stage system with 12.5 J of total energy (8 J on the first stage and 4.5 J on the second), the velocity reaches 8076 m/s. In addition, when 12.5 J of total energy is supplied on the first stage (1000 V on the first stage and 0 V on the second stage), the efficiency is 0.5%. When a similar amount of total energy is supplied for the two stages (800 V on the first stage

Table 4

Data measurement from energy breakdown and peak current when voltage for the first-stage electrodes remains constant at 1000 V.

| V_2 [V] | E_1 [J] | E_2 [J] | E_{tot} [J] | Δt [μ s] | V_{e1} [m/s] | V_{e2} [m/s] | m_a [μ g] | I_{b1} [μ N·s] | I_{b2} [μ N·s] | $I_{b,t}$ [μ N·s] | $I_{sp,1}$ [s] | $I_{sp,2}$ [s] | η_t [%] |
|-----------|-----------|-----------|---------------|-----------------------|----------------|----------------|------------------|-----------------------|-----------------------|------------------------|----------------|----------------|--------------|
| 0 | 12.5 | 0 | 12.5 | 13.2 | 3182 | 0.00 | 12.9 | 41.09 | 0.003 | 41.09 | 324.3 | 0.00 | 0.52 |
| 200 | 12.5 | 0.5 | 13 | 18.4 | 2283 | 0.14 | 17.0 | 38.81 | 2.314 | 41.12 | 232.7 | 0.01 | 0.34 |
| 400 | 12.5 | 2 | 14.5 | 11.1 | 3784 | 0.89 | 10.6 | 40.02 | 9.387 | 49.41 | 385.7 | 0.09 | 0.52 |
| 600 | 12.5 | 4.5 | 17 | 5.7 | 7368 | 2.60 | 5.4 | 40.02 | 14.104 | 54.12 | 751.1 | 0.26 | 0.87 |
| 800 | 12.5 | 8 | 20.5 | 3 | 14000 | 7.47 | 2.9 | 40.02 | 21.362 | 61.38 | 1427.1 | 0.76 | 1.37 |
| 1000 | 12.5 | 12.5 | 25 | 2.15 | 19535 | 15.78 | 2.0 | 40.02 | 32.33 | 72.35 | 1991.3 | 1.61 | 1.56 |

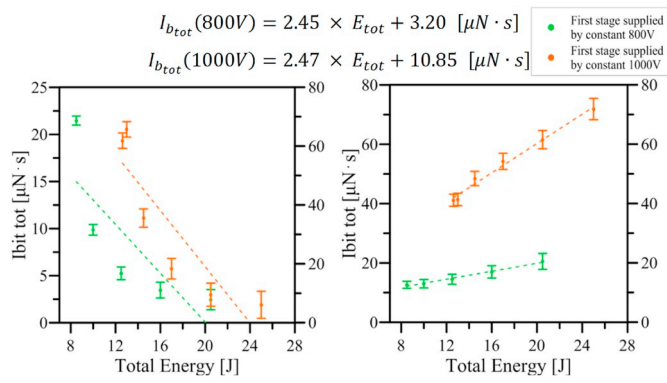


Fig. 5. (a) Discharge delay between the two stages in the function of total energy and (b) thrust-to-power ratio in the function of total energy when first-stage voltage is maintained at 800 V (green) and 1000 V (orange) while the second-stage voltage varies. (For interpretation of the references to colour in this figure legend, the reader is referred to the Web version of this article.)

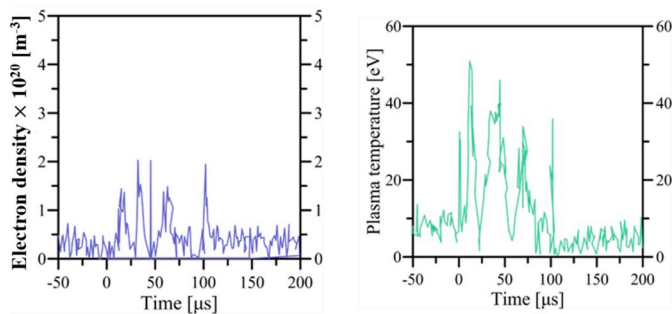


Fig. 6. (a) Electron density and (b) plasma temperature in eV when a discharge is triggered with 1000 V supplied to first-stage electrodes.

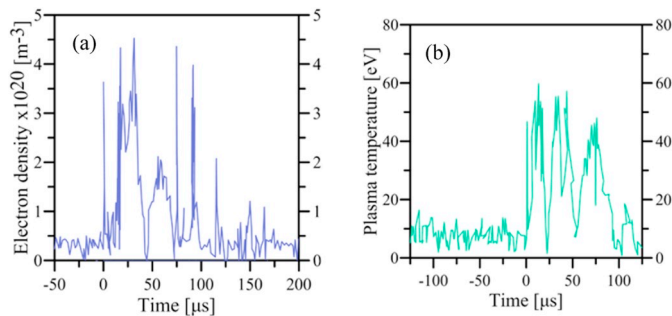


Fig. 7. (a) Electron density and (b) plasma temperature in eV when the two stages discharged with 1000 V and 200 V, respectively.

and 600 V on the second stage), the efficiency increases to 4.4%. Thus, for the same total energy, the velocity and efficiency are greater for a dual-stage PPT than for a single-stage PPT. This pulling force can be

explained by the second-stage electrostatic field (potential difference between plasma and second-stage electrode) that is acting on the upstream plasma bulk, which attracts it toward the exit area.

Fig. 5 presents performance enhancements from adding a second electrode stage to a basic PPT design. When the first-stage energy remains constant and downstream second-stage energy is increasing, the velocity of plasma increases toward the thruster exit. This might result from a pulling force coming from the second stage and acting directly on the plasma when it is coming out of the first stage. This improvement in plasma acceleration is highly reliable and is directly linked to optimization of the ratio between propellant consumption and the increase in total impulse bit of the thruster. Based on Fig. 5 (a) and the plasma flight time between the first and second stages, the first value of the 1000-V curve may be produced by an error in measurement. The semiempirical equations of impulse bit as a function of total energy when the first-stage voltage remains constant at 800 V or 1000 V are expressed as follows.

$$I_{b_{tot}}(800V) = 2.45 \times E_{tot} + 3.20 [\mu N \cdot s]$$

$$I_{b_{tot}}(1000V) = 2.47 \times E_{tot} + 10.85 [\mu N \cdot s]$$

3.3. Plasma density and temperature measurement

Langmuir probe experiments can effectively detect plasma plumes released by a DESPPT prototype. In general, a typical signal acquired by a typical Langmuir probe is too weak to be studied, and an amplifier circuit is inevitably required. In this study, when the energy was high, the voltage and current curves of the triple Langmuir probe were saved directly and without the assistance of any external amplifier circuit. Two cases were examined in order to get an overview and investigate on electron density and temperature variation. The first case supplied 1000 V to the first-stage electrodes of our DESPPT, and the second case supplied 200 V to the second-stage electrodes of our DESPPT.

Figs. 6 and 7 show the plasma density and plasma temperature distribution measured by the triple Langmuir probe for single-stage charged electrodes and dual-stage charged electrodes. The density increased by approximately $2 \times 10^{20} m^{-3}$ when the dual-stage electrodes were charged. The increase in plasma density with the addition of the second-stage electrodes discharged can be explained by two arguments. First, the increase in plasma density can be attributed to the yield of LTA. Basically, in a single PPT, mass ablated late in the reaction does not participate in the final thrust, and thrust is presumably lost by the PPT.

Second, this increase in particle density might be proof of the efficiency of the DESPPT system in accelerating this mass toward the exhaust exit. The system produces thrust but saves propellant and increases the durability of the thruster, leading to a longer lifetime. Alternatively, the increase in plasma density can be explained by other eroded particles from the second-stage electrodes.

3.4. Plasma behavior within the thruster chamber

Fig. 8 presents a photograph of a plasma plume. The luminescence

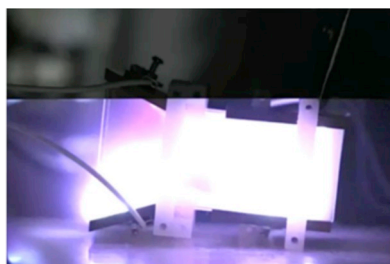
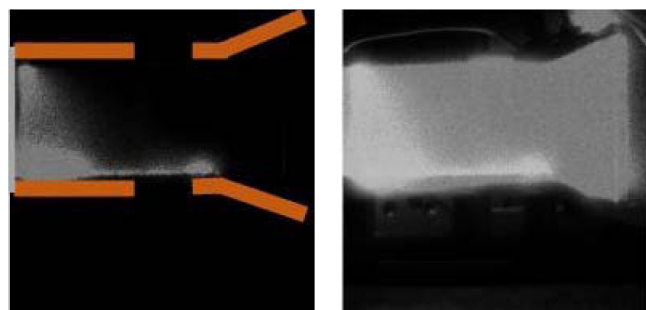


Image with truncation due to the difference between the imaging scanning rate of the camera and the discharging time of the DESPPT.

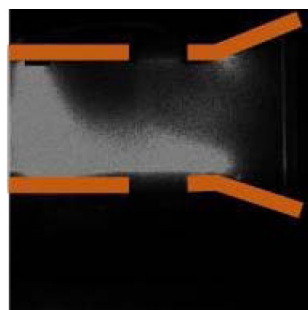
Fig. 8. Photograph of the DESPPT during discharging.



$t1 [\mu s]$



$t1 + 13.88 [\mu s]$



$t2 [\mu s]$



$t2 + 13.88 [\mu s]$



$t1 + 27.76 [\mu s]$



$t1 + 41.64 [\mu s]$



$t2 + 27.76 [\mu s]$



$t2 + 41.64 [\mu s]$



$t1 + 55.52 [\mu s]$



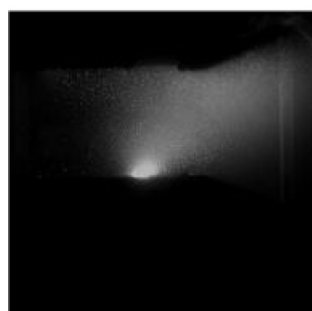
$t1 + 69.4 [\mu s]$



$t2 + 55.52 [\mu s]$



$t2 + 69.4 [\mu s]$



$t1 + 83.26 [\mu s]$



$t1 + 97.16 [\mu s]$

Fig. 9. High-speed camera pictures with filter when discharges are set at 1000 V on the first stage and 1000 V on the second stage (frame speed is set at 72 000 frames per second).

of plasma plume was too bright for the camera, leading to distortion of the image. In addition, this photograph was truncated due to mismatch between the plasma discharging rate and the frame rate of the video camera. To overcome these shortcomings, a high-speed camera was

Fig. 10. High-speed camera pictures with the filter when discharges are set at 800 V in the first stage and 1000 V in the second stage (frame speed is set at 72 000 frames per second).

employed to capture plasma images over short time intervals.

Regarding Fig. 9, the filter allows us to visualize the behavior of flowing particles when a discharge event is triggered at 1000 V on the first stage and 1000 V on the second stage. Based on the picture, the first discharge occurs at $t1 \mu s$. The following picture at $t1 + 13.88 \mu s$ shows the two discharges. Indeed, the two distinct discharge events exhibit a certain time gap. Thus, this Δt is less than $13.88 \mu s$? This observation approximately corresponds to the previous discharge Δt calculation along the voltage breakdown curves.

However, an unexpected phenomenon can be observed: A “V” shape formed between the first and second stages. Because these two stages are charged with the same amount of voltage, the expected bright shape should have been a parallelepiped instead. This might come from a swapping current between the two stages. Indeed, the flowing current from the two following PPT are connected to the same part of the ground. Therefore, it might induce a swap between the initial cathode and anode. This would change the direction of the electromagnetic force acting on the bulk to create this “V” shape.

Verifying the assumption made for Fig. 9, the potential difference

between the cathode and anode is decreased in the first stage and increased in the second stage, as seen in Fig. 10. A new displacement thus takes form, and this seems to be similar for the second stage. When 1000 V and 1000 V are supplied, the displacement seems to be swapped from the first stage and second stage, it is now remaining similar on to the Fig. 9. Assumptions can be made based on the following statement: when decreasing the voltage of the first stage, we can avoid the electrode swapping phenomena.

4. Conclusion

A DESPPT has been prototyped and tested. The Langmuir triple probe revealed differences between single-stage and dual-stage PPTs. It allowed us to measure electron plasma density and temperature in electron-volts. For the single PPT, the density ranged from $1.5 \times 10^{20} \text{ m}^{-3}$ to $2 \times 10^{20} \text{ m}^{-3}$ when the maximum temperature ranged from 50 to 60 eV. For the dual-supplied electrode stage, the density increased from $2 \times 10^{20} \text{ m}^{-3}$ to $3 \times 10^{20} \text{ m}^{-3}$, whereas the temperature of the plasma remained similar. This difference in density reveals that for the same amount of ablated propellant mass, the density increases because of added mass. This added mass in the plasma bulk can serve as the LTA. Peak current data were measured with a high-current monitor. Therefore, we measured and formalized the total impulse bit of the system and exit velocity. Those characteristics, when combined with energy, can be used to assess the efficiency of the thruster.

Appendix

Voltage range for the first stage:

$$V_1 = 500 \text{ to } 1000 \text{ [V]} \quad (28)$$

Voltage range for the second stage:

$$V_2 = 150 \text{ to } 1000 \text{ [V]} \quad (29)$$

Capacitance:

$$C_1 = C_2 = 25 \text{ [\mu F]} \quad (30)$$

It is easy to calculate the energy of the capacitor, resistance, charging time, and frequency with the following equations:

Range for stored energy to supply the first stage:

$$E = \frac{1}{2} C \times V^2 \text{ [J]} \quad (31)$$

$$\text{From } E_{500V1} = 0.5 \times 25 \times 10^{-6} \times 500^2 = 3.125 \text{ [J]} \quad (32)$$

$$\text{To } E_{1000V1} = 0.5 \times 25 \times 10^{-6} \times 1000^2 = 12.5 \text{ [J]} \quad (33)$$

Range for stored energy to supply the second stage:

$$\text{From } E_{150V2} = 0.5 \times 25 \times 10^{-6} \times 150^2 = 0.28125 \text{ [J]} \quad (34)$$

$$\text{To } E_{1000V2} = 0.5 \times 25 \times 10^{-6} \times 1000^2 = 12.5 \text{ [J]} \quad (35)$$

References

- [1] J. Lun, Development of a Vacuum Arc Thruster for Nanosatellite Propulsion, University of Stellenbosch, Stellenbosch, 2009.
- [2] C. Sabol, R. Burns, C.A. McLaughlin, Satellite formation flying design and evolution, Spaceflight mechanics 1999 (1999) 265–284.
- [3] J. Esper, et al., Nano/micro satellite constellations for earth and space science, Acta Astronaut. 52 (9–12) (2003) 785–792.
- [4] J. Kolbeck, et al., μ CAT Micro-propulsion Solution for Autonomous Mobile On-Orbit Diagnostic System, (2016).
- [5] I. Kronhaus, M. Laterza, Y. Maor, Inline Screw Feeding Vacuum Arc Thruster 88 (2017) 043505.
- [6] J.B. Robinson, D.J. Richie, Stabilization and attitude determination methods for falconsat-3, J. Spacecr. Rocket. (2016) 507–519.
- [7] P.J. Wilbur, R.G. Jahn, F.C. Curran, Space electric propulsion plasmas, IEEE Trans. Plasma Sci. 19 (6) (1991) 1167–1179.
- [8] R.L. Burton, P.J. Turchi, Pulsed plasma thruster, J. Propuls. Power 14 (5) (1998) 716–735.
- [9] Y. Chan, et al., Review of thermal pulsed plasma thruster-Design, characterization, and application, Proc. 34th Int. Electr. Propuls. Conf. 2015.
- [10] Cabrera, M., et al. Pulsed Plasma Thrusters: a worldwide review and long yearned classification. in Int. Electr. Propuls. Conf.
- [11] J.K. Ziemer, Performance Scaling of Gas-Fed Pulsed Plasma Thrusters, Princeton University, 2001.
- [12] A. Kakami, et al., Performance study on liquid propellant pulsed plasma thruster, 39th AIAA/ASME/SAE/ASEE Joint Propulsion Conference and Exhibit, American Institute of Aeronautics and Astronautics, 2003.
- [13] H. Koizumi, et al., Effect of solute mixing in the liquid propellant of a pulsed plasma thruster, Vacuum 80 (11) (2006) 1234–1238.
- [14] M. Lau, G. Herdrich, Plasma diagnostic with inductive probes in the discharge channel of a pulsed plasma thruster, Vacuum 110 (2014) 165–171.
- [15] Y. Ou, et al., Experimental investigation on characteristics of pulsed plasma thrusters with the propellant samples of modified PTFE filled Si, Al and Al₂O₃,

- Vacuum 165 (2019) 163–171.
- [16] I.J. Jordan, Electric Propulsion: Which One for My Spacecraft. Space Systems I Course at JHU, Whiting School of Engineering, 2000.
 - [17] G.G. Spanjers, et al., Propellant losses because of particulate emission in a pulsed plasma thruster, *J. Propuls. Power* 14 (4) (1998) 554–559.
 - [18] M. Coletti, R. Marques, S. Gabriel, Design of a two-stage PPT for CubeSat application, Proceedings of the 31st International Electric Propulsion Conference, 2009.
 - [19] L.A. Arrington, et al., A Performance Comparison of Pulsed Plasma Thruster Electrode Configurations, (1997).
 - [20] R. Eckman, et al., Triple Langmuir probe measurements in the plume of a pulsed plasma thruster, *J. Propuls. Power* 17 (4) (2001) 762–771.
 - [21] Y.-H. Li, et al., Plasma behavior in a solid-fed pulsed plasma thruster, *J. Aeronaut. Astronaut. Aviat.* 51 (1) (2019) 31–42.